# Chapter 1
# Three-Dimensional Point Tracking Using UAV-Based Stereo Vision

**Fabio Bottalico, Christopher Niezrecki, and Alessandro Sabato**

**Abstract** Three-dimensional point tracking (3D-PT) is a powerful non-contact method for capturing displacements and deformations in structural health monitoring (SHM) applications. However, its broader adoption is limited by the need for stereo cameras to be rigidly mounted with fixed baselines and calibrated using large, cumbersome targets. These constraints make traditional 3D-PT impractical for large-scale or remote environments where access and setup are challenging. This work introduces a hybrid calibration framework that enables 3D-PT using two independently hovering unmanned aerial vehicles (UAVs), each carrying a single camera. The proposed method fuses real-time GPS and IMU data to dynamically compute extrinsic parameters, eliminating the need for fixed mounts or oversized calibration objects. To address challenges posed by UAV motion and sensor desynchronization, the approach incorporates a homography-based motion compensation technique that corrects for frame-to-frame camera movement using visual features on a planar surface. Experimental results demonstrate that the method achieves sub-centimetre tracking accuracy and a displacement error of less than 2% compared to a stationary ground-based stereo vision system, even under moderate wind disturbances. The ability to perform 3D tracking without fixed baselines or pre-installed calibration targets marks a significant step forward in making 3D-PT more scalable and field-deployable. While the current implementation requires offline compensation for sensor timing mismatches, future developments in real-time synchronization and onboard processing will further enhance its utility for dynamic, large-scale SHM applications.

**Keywords** Digital image correlation · stereo vision · structural health monitoring · three-dimensional point tracking · unmanned aerial vehicles

## Introduction

Over recent years, computer vision techniques have gained prominence in structural health monitoring (SHM), particularly for evaluating a structure's dynamic [1]. Among these, three-dimensional digital image correlation (3D-DIC) and three-dimensional point tracking (3D-PT) have proven effective for measuring displacements in bridges [2], railroads [3], wind turbine blades [4], as well as for system identification [5] and structural dynamics studies [6].

As illustrated in Figure 1a, 3D-DIC and 3D-PT reconstruct the 3D displacement of a moving point **P** by matching its projections captured on the image planes of synchronized stereo cameras. In this work, 3D-PT is considered a subset of 3D-DIC, where a single optical target (e.g., a white circle on a dark background) is tracked instead of a stochastic speckle pattern. Before measurements can be performed, the stereo system must be calibrated to determine the intrinsic parameters (image center, focal length, and lens distortion) and the extrinsic parameters (relative orientation and distance between cameras). As shown in Figure 1b, this is typically achieved by capturing stereo images of a coded calibration object [7], such as a cross or a checkerboard with dimensions comparable to the structure under study. Because extrinsic parameters depend on the camera position, any configuration change invalidates the calibration and requires recompilation, a cumbersome process for large-scale systems. To avoid this, the cameras are mounted on a rigid bar to eliminate relative motion [1]. This requirement for scale-sensitive calibration and rigid mounting significantly limits the practicality of 3D-DIC and 3D-PT for large-scale SHM applications.

Fabio Bottalico · Christopher Niezrecki · Alessandro Sabato
Department of Mechanical and Industrial Engineering, University of Massachusetts Lowell, 1 University Avenue, Lowell, MA 01854
e-mail: Fabio_Bottalico@uml.edu; Christopher_Niezrecki@uml.edu; Alessandro_Sabato@uml.edu

© The Author(s), under exclusive license to River Publishers 2026

Kristin B. Zimmerman, PhD (eds.), *Computer Vision and SLDV for Structural Dynamics, 2026, Vol. 6*, Conference Proceedings of the Society for Experimental Mechanics Series, https://doi.org/10.13052/rp-9788743814177

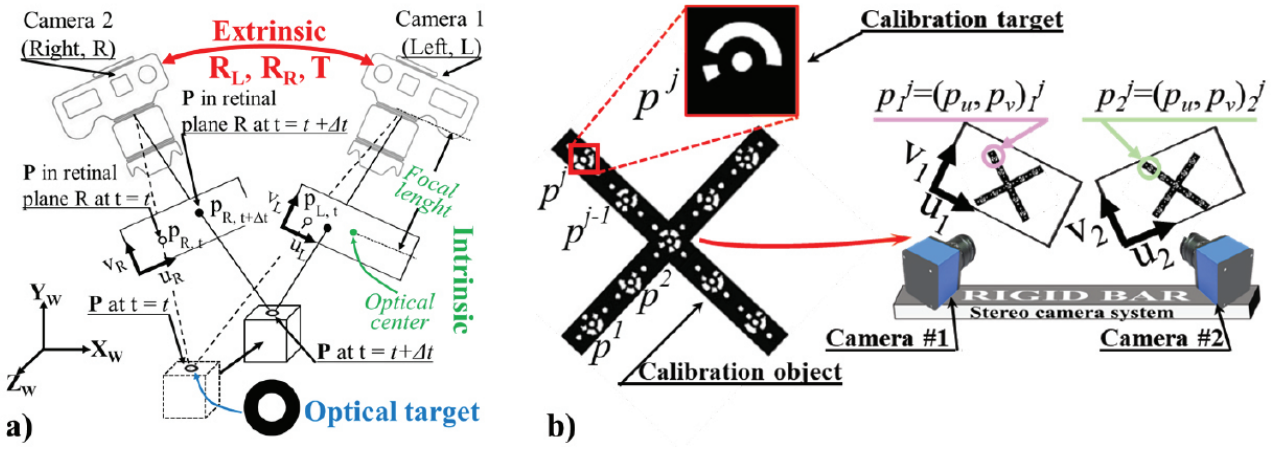



**Fig. 1** Operational principles of 3D-PT: a) tracking a moving point **P** from its projection in the two retinal planes of the stereo camera system, and b) calibration using a calibration object with coded targets as seen from the two cameras.

Unmanned aerial vehicles (UAVs) have recently become powerful tools for inspecting hard-to-reach locations. UAV-based computer vision has been applied to generate 3D static maps using Structure-from-Motion (SfM) [8] and simultaneous localization and mapping (SLAM) [9], as well as to detect cracks, corrosion, and other forms of deterioration in bridges [10], dams [11], towers [12], and buildings [13] through visual and thermal imagery [14]. Beyond static mapping, UAV-mounted cameras are increasingly used for dynamic measurements. UAV oscillations during flight introduce motion artifacts, necessitating the use of fixed background points to compensate for UAV motion and recover structural displacements. This approach has been applied to experiments on trusses [15], beams [16], panels [17], and toy bridges [18], as well as in field applications on towers [19] and full-scale bridges [20]. Despite these successes, single-camera systems remain limited to 2D measurements.

To address this limitation, researchers have integrated UAVs with 3D-DIC by rigidly mounting two synchronized cameras on a single drone. Such systems have been tested on wind turbine blades [21], trusses [22], and beams [23], and deployed for crack monitoring in bridges [24]. Yet, their practicality is constrained by the short stereo baseline (typically 0.5–1 m) that a single UAV can accommodate, which restricts the field of view (FOV) to less than 2 m. To overcome these constraints, this research proposes a novel method that utilizes two independently hovering UAVs, each equipped with a single camera, to form a fully adaptable, non-fixed-baseline stereo vision system, as illustrated in Figure 2. The approach builds on prior work in sensor-based stereocamera calibration [25–27] and leverages the inertial measurement units (IMUs) and global navigation satellite systems (GNSS) integrated into commercial UAV platforms.

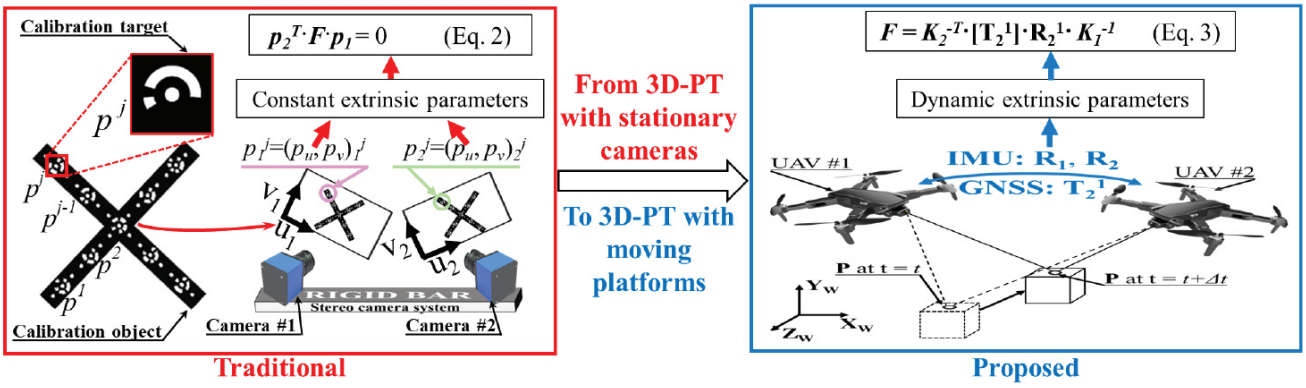



**Fig. 2** Contributions of this study relative to current 3D-PT practices: extrinsic parameters are dynamically updated from UAV onboard IMU and GNSS data instead of being fixed from calibration target reprojections with rigidly mounted cameras.

This study presents the first proof-of-concept for dynamically estimating the extrinsic parameters between two cameras mounted on independent UAVs in real time. Experimental results show that the method can track the 3D displacement of

a moving target with ∼98% accuracy relative to a stationary, ground-mounted stereocamera system. The remainder of this paper is organized as follows. Section 2 introduces the mathematical framework for dynamic recalibration. Sections 3 and 4 describe the experimental setup and validation results, respectively. Section 5 concludes with key findings and directions for future research.

## Methodology

The pinhole camera model forms the basis of photogrammetry and computer vision techniques. It describes how a 3D point $\boldsymbol{P} = [P_x, P_y, P_z]^T$, defined in a global reference frame *W*, is projected onto the camera's image plane as a 2D point $\boldsymbol{p} = [p_u, p_v]^T$ as expressed in Equation (1):

$$\begin{bmatrix} p_u \\ p_v \\ 1 \end{bmatrix} = \begin{bmatrix} f_x & \theta & c_x \\ 0 & f_y & c_y \\ 0 & 0 & 1 \end{bmatrix} \begin{bmatrix} R_{xx} & R_{xy} & R_{xz} & T_x \\ R_{yx} & R_{yy} & R_{yz} & T_y \\ R_{zx} & R_{zy} & R_{zz} & T_z \end{bmatrix}_W \begin{bmatrix} P_x \\ P_y \\ P_z \\ 1 \end{bmatrix}_W \tag{1}$$

Here, the 3x3 matrix intrinsic parameters matrix $\boldsymbol{K}$ contains information about the camera's focal length $(f_x, f_y)$, the coordinates of the optical centre $(c_x, c_y)$, and the skew factor $\theta$. For the applications considered in this work, $\boldsymbol{K}$ is treated as constant. The 3x4 matrix $\boldsymbol{R|T}$ describes the extrinsic parameters and consists of the nine components of a rotation matrix $\boldsymbol{R}$ and the translation vector $\boldsymbol{T}$. Calibration is traditionally performed by solving Equation (1) for $\boldsymbol{K}$ and $\boldsymbol{R|T}$ using multiple images of a calibration target with known geometry (i.e., the coordinates of all points $\boldsymbol{p}^j$ shown in Figure 1b). When a 3D point $\boldsymbol{p}^j$ is projected onto the two image planes, its representation appears as points $\boldsymbol{p}_1{}^j$ and $\boldsymbol{p}_2{}^j$ in the two cameras, connected by a relationship expressed as:

$$\boldsymbol{p_2^T}\ \boldsymbol{F}\ \boldsymbol{p_1} = 0 \tag{2}$$

Here, **F** is a 3x3 singular matrix of rank two, known as the fundamental matrix, which includes the intrinsic and extrinsic parameters of the stereo camera as:

$$\boldsymbol{F} = \boldsymbol{K}_2^{-T}\ \left[\boldsymbol{T_2^1}\right]_x \boldsymbol{R_2^1}\ \boldsymbol{K}_1^{-1} \tag{3}$$

In Equation (3), $\boldsymbol{K}_1{}^{-1}$ is the inverse of the intrinsic parameters' matrix of Camera 1 and $\boldsymbol{K}_2{}^{-T}$ is the transpose of the intrinsic parameter matrix of Camera 2. $[\boldsymbol{T}_2{}^1]_x$ is the cross-product matrix of the translation vector $\boldsymbol{T}_2{}^1$ (i.e., the relative distance between the cameras), while $\boldsymbol{R}_2{}^1$ is the relative rotation matrix of Camera 2 expressed in Camera 1's reference frame. Traditional target-based calibration methods compute $\boldsymbol{F}$ directly from Equation (2) by identifying multiple pairs of corresponding points $(\boldsymbol{p}_1, \boldsymbol{p}_2)_i$ in stereo images of a calibration object. The intrinsic and extrinsic parameters are then extracted from the decomposition of $\boldsymbol{F}$ using Equation (2). By contrast, sensor-based calibration methods bypass this step and rely directly on Equation (3), where $\mathbf{R}_2{}^1$ and $\mathbf{T}_2{}^1$ are measured from the UAVs' GNSS and IMU sensors (see Figure 2), as defined in Equations (4) and (5).

$$\begin{cases} T_1^W(t) = N * lla2ned\left(T_1^{WGS84}(t) - T_1^{WGS84}(0)\right) \\ T_2^W(t) = N * lla2ned\left(T_2^{WGS84}(t) - T_1^{WGS84}(0)\right) \end{cases} \tag{4}$$

$$\boldsymbol{R}_i^W = \begin{bmatrix} cos(\alpha_i) & -sin(\alpha_i) & 0 \\ sin(\alpha_i) & cos(\alpha_i) & 0 \\ 0 & 0 & 1 \end{bmatrix} \begin{bmatrix} cos(\beta_i) & 0 & sin(\beta_i) \\ 0 & 1 & 0 \\ -sin(\beta_i) & 0 & cos(\beta_i) \end{bmatrix} \begin{bmatrix} 1 & 0 & 0 \\ 0 & cos(\gamma_i) & -sin(\gamma_i) \\ 0 & sin(\gamma_i) & cos(\gamma_i) \end{bmatrix} \tag{5}$$

In Equation (4), the translation vectors $\mathbf{T}_i{}^W$ of the two cameras are obtained from the GNSS sensors, which are reported in WGS84 latitude–longitude–altitude (LLA) coordinates and then converted into the North-East-Down (NED) reference frame using MATLAB's *lla2ned()* function. In Equation (5), $\alpha$, $\beta$, and $\gamma$ are the roll, yaw, and pitch angles measured by the IMUs on the UAVs, following the NED convention.

In practice, however, the GNSS, IMU, and camera sensors on commercial UAVs typically operate at different or insufficient sampling rates, which complicates the data processing. For instance, high-frequency oscillations of a hovering UAV are not captured by the GNSS, and GNSS measurements are often not perfectly synchronized with the camera. These limitations introduce errors in the estimation of extrinsic parameters, leading to inaccuracies in the triangulated positions of tracked points. To mitigate these issues, the images themselves must be exploited to refine the estimation of extrinsic parameters. A practical solution is motion correction via homography, as described in Equation (6).

$$\boldsymbol{h_2} = \boldsymbol{H}\boldsymbol{h_1} \tag{6}$$

Here, $\boldsymbol{H}$ is a non-singular 3x3 homogeneous matrix, and $\boldsymbol{h}_1$ and $\boldsymbol{h}_2$ are the points in the image selected as a reference. Although similar in form, Equation (6) imposes different constraints than Equation (2). By matching feature points between an image acquired at $t = 0$ and another at $t = t_i$, Equation (6) can be solved for $\boldsymbol{H}$. The resulting homography is then fused with the IMU–GNSS data to compensate for the relative motion of the two UAVs. In summary, the calibration procedure involves two steps: first, estimating the extrinsic parameters of the stereo system using IMU and GNSS sensors; and second, applying the homography method to correct any residual motion between the cameras.

## Experimental Setup

Two tests were conducted to evaluate the accuracy of the proposed method for tracking the 3D displacement of an object using two cameras mounted on independent UAVs. The setup employed two DJI Matrice 300 RTK UAVs, each equipped with a gimbal-mounted camera. UAV 1 carried a Sony A7R-V with a 35 mm fixed focal length lens (UAV-Camera 1), while UAV 2 carried a DJI Zenmuse XT2 with an 8 mm fixed focal length lens. The intrinsic parameters of both cameras were calibrated beforehand, and because the lenses are fixed, the intrinsic matrices $\boldsymbol{K}_1$ and $\boldsymbol{K}_2$ remained constant across all measurements.

Test 1 evaluated the feasibility of estimating the extrinsic parameters of a stereovision system by combining real-time kinematic global navigation satellite system (RTK-GNSS) data for the translation vector $\boldsymbol{T}$ with orientation data from the high-sensitivity IMUs embedded in the UAVs' gimbals for the rotation matrix $\boldsymbol{R}$. For this experiment, the UAVs were positioned as shown in Figure 3a, forming a stereovision system with an approximate baseline of 8 m and a working distance of 15 m. The UAV-mounted cameras captured stereo image sequences of a calibration checkerboard while simultaneously recording GNSS and IMU data. The extrinsic parameters derived from the UAV sensors were then compared with those obtained from image-based calibration. Test 1 was designed to minimize synchronization-related errors and to assess the geometric performance of the proposed approach without interference from timing mismatches among the GNSS, IMU, and cameras.

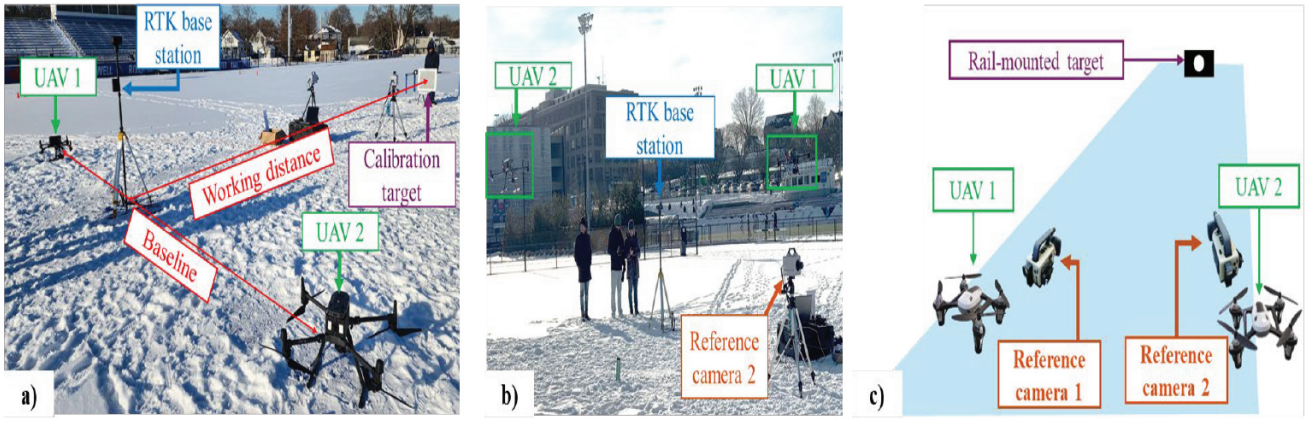



**Fig. 3** Experimental setup: a) Test 1, showing the two UAVs, the RTK base station, and the calibration checkerboard used for image-based calibration, b) UAVs hovering behind the ground-based cameras during Test 2, and c) schematic (not to scale) of the experimental setup for Test 2.

Test 2 evaluated the feasibility of applying the proposed calibration method to track a moving object using two cameras mounted on independently hovering UAVs. The same UAVs from Test 1 were flown in manual mode, each maintaining an altitude of ∼2.5 m. As shown in Figures 3b and 3c, the UAVs were positioned behind two ground-based cameras that served as a reference system. A rail-mounted sliding carriage was installed on supports, with a high-contrast optical target attached to the slider. The target was translated from right to left in 12 increments. At each position, both the ground-based stereocamera system and the UAV-mounted cameras captured five images. During acquisition, wind gusts of up to 8 $m \cdot s^1$ caused significant UAV oscillations. The RTK-GNSS and IMU data collected from the two UAVs were again used to compute the extrinsic parameters of the stereovision system formed by UAV 1 and UAV 2.

## Results

The results of **Test 1** are summarized in Table 1, comparing the extrinsic parameters estimated with the GNSS–IMU system against those from conventional image-based calibration. As shown in Table 1, the extrinsic parameters obtained with the proposed calibration method closely match those from traditional image-based calibration, particularly in the angular measurements. The yaw angle $\beta$ (i.e., the separation angle of the two cameras in the horizontal plane through their optical centres) differs by only 0.012°, corresponding to a relative error of 0.037%, demonstrating excellent agreement. The pitch $\alpha$ and roll $\gamma$ angles from the proposed method are nearly zero, reflecting both the parallel alignment of the cameras to the ground and the effectiveness of the gimbal stabilization. By contrast, the image-based calibration produced nonzero pitch and roll values, likely due to the calibration object being too small relative to the field of view (a well-known scale sensitivity issue that this work aims to overcome).

**Table 1** Extrinsic parameters of UAV–Camera 2 relative to UAV–Camera 1 from image-based and GNSS–IMU calibration in Test 1.

| | $\alpha$ (°) | $\beta$ (°) | $\gamma$ (°) | $T_X$ (*mm*) | $T_Y$ (*mm*) | $T_Z$ (*mm*) |
|---|---|---|---|---|---|---|
| **Image-based** | 2.275 | 32.249 | -0.940 | -8012.50 | 34.53 | 2009.60 |
| **Proposed** | 0.022 | 32.261 | 0.007 | -8116.30 | 304.79 | 2041.20 |
| **Difference** | 2.253 | -0.012 | -0.947 | 103.80 | -270.26 | -31.60 |

The translation components also show strong consistency. Differences in the horizontal $T_X$ and vertical $T_Z$ components of the translation vector correspond to errors of 1.29% and 1.57%, respectively. The only significant discrepancy appears in the lateral component $T_Y$, where the methods differ by 270.26 mm. This deviation stems from the altitude quantization resolution of the RTK-GNSS system (∼304.79 mm, or 1 ft) used on the commercial UAV platform. Crucially, this reflects a hardware constraint rather than a limitation of the proposed method.

Figure 4 presents the results of tracking the optical target (see Figure 3c) with two cameras mounted on independent UAVs. Two cases are shown: *1)* extrinsic parameters estimated using only GNSS–IMU data, and *2)* extrinsic parameters

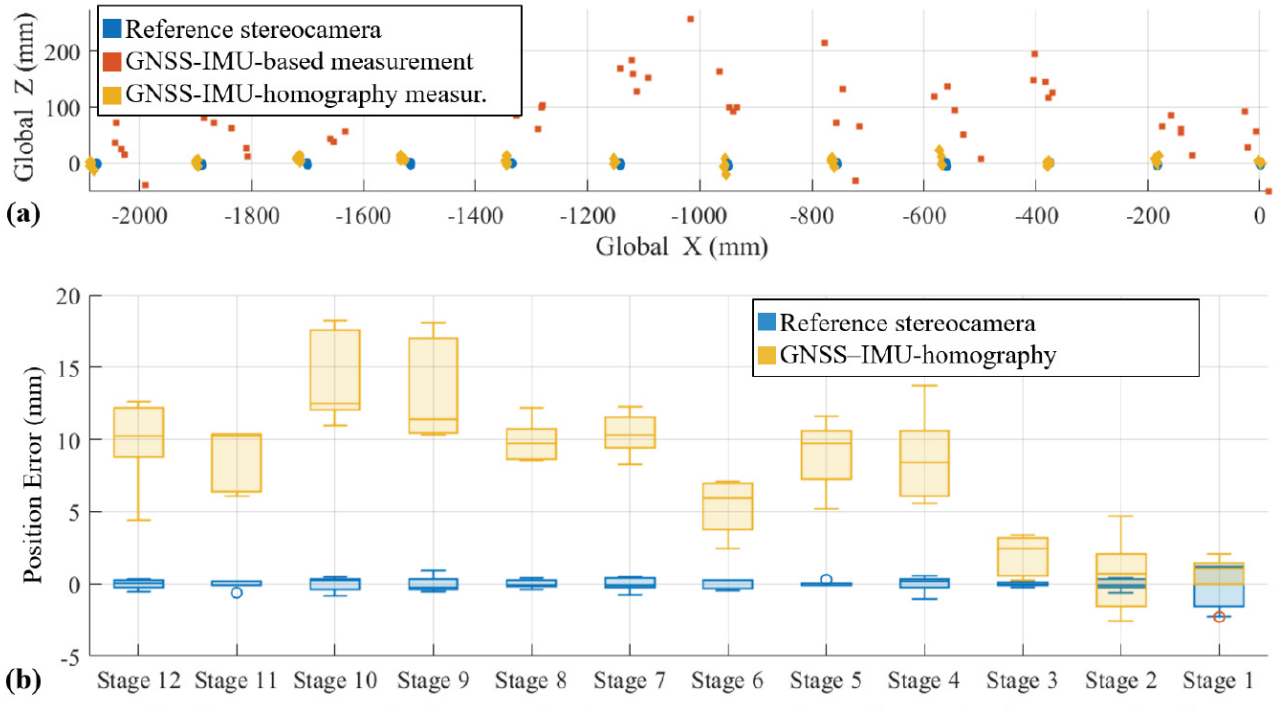



**Fig. 4** Displacement of the optical target: a) locations before and after motion compensation, showing improved alignment, and b) whisker plot of deviations from the ground-based reference.

refined using GNSS–IMU data with homography-based motion compensation. The compensation approach significantly improves accuracy, reducing errors to the centimetre-level (Figure 4a), as the measured displacement converges more closely to the ground-based stereocamera reference. Without compensation, GNSS–IMU measurements deviate from the reference by up to $\pm$50 mm in mean displacement, with standard deviations of 50 to 100 mm. In contrast, GNSS–IMU–homography results closely match the reference values (golden dots compared to red dots in Figure 4a).

The whisker plot in Figure 4b zooms in on the results shown in Figure 4a and further confirms this improvement: the maximum absolute mean displacement error decreases to just 15 mm, compared to the $\pm$50 mm range observed without compensation. At Stage 10, where the total displacement is 1700 mm, this corresponds to a relative error of only 0.88%. At Stage 12, with a total displacement of 2090 mm, the 10 mm error yields an even smaller relative error of 0.48%. In addition to improved accuracy, the precision of the UAV-based measurements increased substantially. The standard deviation of displacement dropped from 50-100 mm to 5-10 mm, representing an order-of-magnitude enhancement. These results clearly demonstrate the effectiveness of the proposed motion compensation method in mitigating UAV-induced errors during 3D tracking.

## Conclusion

A novel calibration method is presented for 3D motion tracking using two independently hovering UAVs, each carrying a camera. Unlike conventional 3D-PT, which requires rigidly mounted cameras and large calibration targets, the proposed approach dynamically estimates extrinsic parameters by combining RTK-GNSS and IMU data and applies homography to compensate for UAV-induced instabilities. This is the first demonstration of stereo vision calibration and 3D-PT performed with two moving UAVs rather than fixed cameras.

Two field tests validated the method. In Test 1, the extrinsic parameters estimated using the proposed GNSS–IMU approach closely matched those obtained from traditional image-based calibration, with angular deviations of nearly zero and translation errors of less than 2%. In Test 2, a moving optical target was tracked using the UAV-mounted cameras. While raw GNSS and IMU data introduced errors due to sensor desynchronization, incorporating homography-based motion compensation reduced the error to below 1% and improved precision by an order of magnitude.

Overall, the proposed method achieves accuracy comparable to conventional calibration techniques while offering greater flexibility and scalability. By removing the need for rigid bars and calibration panels, it enables 3D tracking in scenarios previously impractical for 3D-PT. Although the current accuracy does not yet meet the millimeter-level demands for SHM, this study establishes a new pathway for UAV-based 3D-PT. Future work should prioritize improving sensor synchronization and integrating higher-rate sensors to enhance reliability and achieve the precision required for full-scale SHM deployment.

**Acknowledgments** This material is based upon work supported by the National Science Foundation (NSF) under Grant Number 2440348 - *CAREER: Enhancing Measurements of Dynamic Features in Large-Scale Structures via Three-Dimensional Aerial Stereovision*. Any opinions, findings, and conclusions or recommendations expressed in this material are those of the authors and do not necessarily reflect the views of the National Science Foundation.

## References

1. B. Pan, "Digital image correlation for surface deformation measurement: historical developments, recent advances and future goals," Measurement Science and Technology, vol. 29, no. 8, p. 082001, 2018.
2. L. Ngeljaratan and M. A. Moustafa, "Structural health monitoring and seismic response assessment of bridge structures using target-tracking digital image correlation," Engineering Structures, vol. 213, p. 110551, 2020.
3. A. Sabato and C. Niezrecki, "Feasibility of Digital Image Correlation for railroad tie inspection and ballast support assessment," Measurement, vol. 103, pp. 93-105, 2017.
4. P. Poozesh, A. Sabato, A. Sarrafi, C. Niezrecki, P. Avitabile, and R. Yarala, "Multicamera measurement system to evaluate the dynamic response of utility-scale wind turbine blades," Wind Energy, vol. 23, no. 7, pp. 1619-1639, 2020.
5. M. Shafiei Dizaji, M. Alipour, and D. K. Harris, "Leveraging Full-Field Measurement from 3D Digital Image Correlation for Structural Identification," Experimental Mechanics, vol. 58, pp. 1049-1066, 2018.
6. D. Gorjup, J. Slavič, and M. Boltežar, "Frequency domain triangulation for full-field 3D operating-deflection-shape identification," Mechanical Systems and Signal Processing, vol. 133, 2019.
7. Z. Zhang, "A flexible new technique for camera calibration," IEEE Transactions on Pattern Analysis and Machine Intelligence, vol. 22, no. 11, pp. 1330-1334, 2000.
8. S. Jiang, C. Jiang, and W. Jiang, "Efficient structure from motion for large-scale UAV images: A review and a comparison of SfM tools," ISPRS Journal of Photogrammetry and Remote Sensing, vol. 167, pp. 230-251, 2020.

9. A. Gupta and X. Fernando, “Simultaneous Localization and Mapping (SLAM) and Data Fusion in Unmanned Aerial Vehicles: Recent Advances and Challenges,” Drones, vol. 6, no. 4, p. 85, 2022.
10. S. Feroz and S. Abu Dabous, “UAV-Based Remote Sensing Applications for Bridge Condition Assessment,” Remote Sensing, vol. 13, no. 9, p. 1809, 2021.
11. S. Zhao, F. Kang, J. Li, and C. Ma, “Structural health monitoring and inspection of dams based on UAV photogrammetry with image 3D reconstruction,” Automation in Construction, vol. 130, p. 103832, 2021.
12. H. Wang, H. Zhou, H. Liu, Z. Huang, and M. Feng, "Research on Determining the Inspection Point of Multirotor UAV Power Tower," Mathematical Problems in Engineering, vol. 2021, no. 1, p. 8894055, 2021.
13. T. Rakha and A. Gorodetsky, “Review of Unmanned Aerial System (UAS) applications in the built environment: Towards automated building inspection procedures using drones,” Automation in Construction, vol. 93, pp. 252-264, 2018.
14. S. Dabetwar, N. N. Kulkarni, M. Angelosanti, C. Niezrecki, and A. Sabato, “Sensitivity analysis of unmanned aerial vehicle-borne 3D point cloud reconstruction from infrared images,” Journal of Building Engineering, vol. 58, p. 105070, 2022.
15. G. Chen, Q. Liang, W. Zhong, X. Gao, and F. Cui, “Homography-based measurement of bridge vibration using UAV and DIC method,” Measurement, vol. 170, p. 108683, 2021.
16. G. Liu, J. Luo, Q. Yang, S.-s. Law, and C. He, “Non-contact Structural Displacement Measurement using UAV and DIC with Non-coplanar Fixed Region of Interest,” Measurement, vol. 242, p. 115936, 2025.
17. Y. Weng, J. Shan, Z. Lu, X. Lu, and B. F. Spencer Jr., “Homography-based structural displacement measurement for large structures using unmanned aerial vehicles,” Computer-Aided Civil and Infrastructure Engineering, vol. 36, no. 9, pp. 1114-1128, 2021.
18. Z. Wu, G. Chen, Q. Ding, B. Yuan, and X. Yang, “Three-Dimensional Reconstruction-Based Vibration Measurement of Bridge Model Using UAVs,” Applied Sciences, vol. 11, no. 11, p. 5111, 2021.
19. H. Habeenzu, P. McGetrick, S. Taylor, and D. Hester, “UAS-based bridge displacement measurement using two cameras with non-overlapping fields of view,” Automation in Construction, vol. 167, p. 105687, 2024.
20. Y. Han, G. Wu, and D. Feng, “Vision-based displacement measurement using an unmanned aerial vehicle,” Structural Control and Health Monitoring, vol. 29, no. 10, p. e3025, 2022.
21. A. Khadka, B. Fick, A. Afshar, M. Tavakoli, and J. Baqersad, “Non-contact vibration monitoring of rotating wind turbines using a semi-autonomous UAV,” Mechanical Systems and Signal Processing, vol. 138, p. 106446, 2020.
22. G. Lavezzi, M. Ciarcià, K. Won, and M. Tazarv, “A DIC-UAV based displacement measurement technique for bridge field testing,” Engineering Structures, vol. 308, p. 117951, 2024.
23. M. Kalaitzakis, N. Vitzilaios, D. C. Rizos, and M. A. Sutton, “Drone-Based StereoDIC: System Development, Experimental Validation and Infrastructure Application,” Experimental Mechanics, vol. 61, no. 6, pp. 981-996, 2021.
24. D. Reagan, A. Sabato, and C. Niezrecki, “Feasibility of using digital image correlation for unmanned aerial vehicle structural health monitoring of bridges,” Structural Health Monitoring, vol. 17, no. 5, pp. 1056-1072, 2018.
25. A. Sabato, N. A. Valente, and C. Niezrecki, “Development of a Camera Localization System for Three-Dimensional Digital Image Correlation Camera Triangulation,” IEEE Sensors Journal, vol. 20, no. 19, pp. 11518-11526, 2020.
26. F. Bottalico, C. Niezrecki, K. Jerath, Y. Luo, and A. Sabato, “Sensor-Based Calibration of Camera’s Extrinsic Parameters for Stereophotogrammetry,” IEEE Sensors Journal, vol. 23, no. 7, pp. 7776-7785, 2023.
27. Bottalico, F., Valente, N. A., Niezrecki, C., Jerath, K., Luo, Y., & Sabato, A. (2025). Rapid 3D Camera Calibration for Large-Scale Structural Monitoring. Remote Sensing, 17(15), 2720.